Nano Research

Open Access

Research Article

Fluorinated MXene-engineered LiF-rich solid electrolyte interphase and hierarchical confinement strategy enabling high performance micro-sized silicon anodes

Lin Sun[1,2] ✉, Lijun Wang[1,2], Tianqi Wang[1], Yanyan Liu[1], Yunjing Qiao[1], Xuetao Lu[1], Miao Qi[3], and Zhong Jin[2] ✉

[1] *School of Chemistry and Chemical Engineering, Yancheng Institute of Technology, Yancheng 224051, China*
[2] *State Key Laboratory of Coordination Chemistry, MOE Key Laboratory of Mesoscopic Chemistry, MOE Key Laboratory of High Performance Polymer Materials and Technology, Jiangsu Key Laboratory of Green Energy Catalysis and Intelligent Chemical Engineering, Suzhou Key Laboratory of Green Intelligent Manufacturing of New Energy Materials and Devices, Tianchang New Materials and Energy Technologies Research Center, Institute of Green Chemistry and Engineering, School of Chemistry and Chemical Engineering, Nanjing University, Nanjing, Jiangsu 210023, China*
[3] *Yancheng Polytechnic College, Yancheng 224005, China*

Cite this article: *Nano Research*, **2026**, *19*, 94908024. https://doi.org/10.26599/NR.2025.94908024

ABSTRACT: Silicon (Si) anodes, despite their exceptional theoretical capacity (~ 4200 mAh·g^{-1}), face critical challenges, including severe volumetric expansion (> 300%) during lithiation and poor intrinsic conductivity, resulting in structural pulverization and unstable solid electrolyte interphase (SEI) formation. This work demonstrates a hierarchical confinement strategy integrating self-assembly and chemical vapor deposition (CVD) to construct microporous silicon-based composite anode material (mpSi-MGC) synergistically encapsulated by few-layer $Ti_3C_2T_x$ (T = F, O, and OH) MXene, reduced graphene oxide (rGO), and CVD carbon coating. The multi-confinement architecture not only enhances mechanical stability but also optimizes electron (e^-)/lithium ions (Li^+) transport kinetics. Systematic *ex situ* analysis reveals that fluorine-functionalized groups in $Ti_3C_2T_x$ significantly boost Li^+ diffusion coefficients by promoting LiF-rich SEI formation, while the exterior CVD-carbon coating further stabilizes the hybrid structure. The optimized mpSi-MGC delivers exceptional Li storage performance: a high reversible initial capacity of 1800 mAh·g^{-1} at 0.2 A·g^{-1}, remarkable cyclability with 992 mAh·g^{-1} retained after 200 cycles at 1.0 A·g^{-1}, and superior rate capability (818 mAh·g^{-1} at 3 A·g^{-1}). This multi-scale confinement design effectively mitigates volume expansion in micron-sized Si while enhancing e^-/Li^+ conductivity, offering a promising paradigm for developing high-energy-density lithium-ion batteries (LIBs) through rational structural engineering and interfacial optimization.

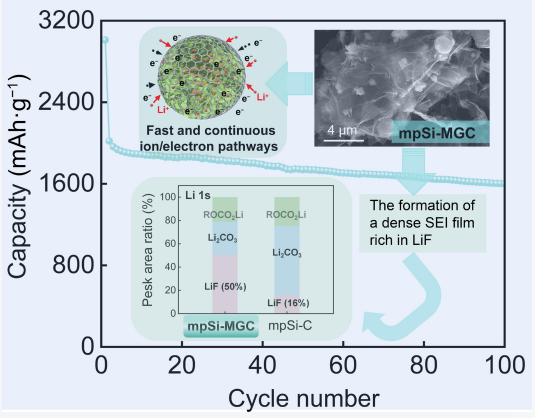

KEYWORDS: micro-sized silicon, anode, MXene, solid electrolyte interphase (SEI), lithium-ion battery

1 Introduction

The ongoing global energy transition and rapid development of electric vehicles and portable electronics have propelled lithium-ion batteries (LIBs) with high energy density and long-term cyclability to the forefront of energy storage research [1–3]. Silicon (Si) has emerged as a highly promising anode material due to its exceptional theoretical capacity (approximately 10-fold higher than graphite), natural abundance, and established industrial production capabilities [4–7]. However, two fundamental challenges impede practical implementation of Si-based anodes: (1) The substantial volumetric fluctuations (> 300%) during (de)lithiation induce severe mechanical stress at both particle and electrode levels, leading to structural pulverization, active material detachment, and consequent rapid capacity degradation [1, 8]; (2) the inherently low electrical conductivity of Si restricts e^-/Li^+ transport kinetics, resulting in unsatisfactory rate performance [9–11].

To address these limitations, researchers have developed

Received: July 18, 2025; **Revised:** August 24, 2025
Accepted: August 31, 2025

✉Address correspondence to Lin Sun, sunlin@nju.edu.cn; Zhong Jin, zhongjin@nju.edu.cn

multifaceted strategies, including Si nanostructuring [12, 13], composite material engineering [14–17], artificial solid electrolyte interphase (SEI) films [18–20], and conductive network architecture [21–23]. Carbon-based composites demonstrate particular effectiveness by simultaneously enhancing conductivity and accommodating volume changes while improving mechanical integrity [24]. However, conventional carbon coatings often fail to reconcile the conflicting requirements of efficient charge transport and robust mechanical stability [25]. Recent advances highlight the potential of two-dimensional (2D) materials like graphene and MXenes (transition metal carbides/nitrides) for Si anode modification [26–28]. Graphene contributes exceptional electrical conductivity and mechanical reinforcement, whereas MXenes (e.g., $Ti_3C_2T_x$) combine metallic conductivity with superior ionic transport facilitated by surface functional groups (T = F, O, and OH) [29, 30]. The synergistic integration of graphene and MXenes with micrometer-sized Si (mSi) may enable composite anodes with optimized charge transfer kinetics and mechanical resilience [31–34].

In this study, we developed a hierarchical Si-based composite anode through acid etching of commercial $Al_{60}Si_{40}$ alloy to obtain porous mSi (mpSi), followed by synergistic modification with reduced graphene oxide (rGO) and $Ti_3C_2T_x$ MXene, and final encapsulation via CVD carbon coating. The ternary architecture leverages graphene's superior electron transport and MXene's ionic conductivity to enhance charge transfer kinetics, while the combined mechanical strength of 2D materials and conformal carbon coating effectively mitigates volume expansion and suppresses parasitic reactions. Additionally, the F groups on the surface of $Ti_3C_2T_x$ can effectively participate in the formation of the SEI film, constructing an SEI film rich in LiF, which significantly promotes Li^+ transport. The optimized microporous silicon-based composite anode material (mpSi-MGC) demonstrates remarkable electrochemical performance, delivering a reversible capacity of 1600 mAh·g^{-1} at 0.2 A·g^{-1} and maintaining 992 mAh·g^{-1} after 200 cycles at 1 A·g^{-1}. This multiscale engineering strategy provides new insights for developing high-performance Si-based anode systems.

2 Experimental

2.1 Preparation of few-layer $Ti_3C_2T_x$ MXene dispersion

To synthesize few-layer $Ti_3C_2T_x$ MXene, 1 g of lithium fluoride (LiF) was dissolved in 20 mL of 9 M hydrochloric acid (HCl) under continuous stirring at 40 °C. Subsequently, 1 g of Ti_3AlC_2 powder was gradually added to the solution, and the reaction mixture was stirred for 24 h to selectively etch the aluminum (Al) layers from the Ti_3AlC_2 precursor. The resulting product was washed repeatedly with deionized water via centrifugation until the supernatant reached a pH of 6. The precipitate was then vacuum-dried at 60 °C overnight to obtain multilayered $Ti_3C_2T_x$. To exfoliate the multilayered $Ti_3C_2T_x$ into few-layer $Ti_3C_2T_x$ MXene, the dried powder was dispersed in 50 mL of deionized water and subjected to probe sonication for 30 min. The dispersion was centrifuged at 3500 rpm for 30 min to remove unexfoliated or thick multilayered precipitates, yielding a stable colloidal suspension of few-layer $Ti_3C_2T_x$ MXene.

2.2 Synthesis of micro-sized silicon (mpSi)

Micro-sized silicon was fabricated by chemically etching a silicon-aluminum alloy ($Al_{60}Si_{40}$). Specifically, 5 g of the alloy powder was immersed in an appropriate volume of 3 M HCl solution under vigorous stirring for 20 h to remove the Al phase. After etching, the product was washed sequentially with deionized water and anhydrous ethanol through multiple centrifugation cycles until the supernatant became neutral. The purified material was then vacuum-dried overnight at 60 °C to obtain the final mpSi.

2.3 Synthesis of mpSi-MGC

A 10 mg·mL^{-1} GO dispersion was first prepared by ultrasonically dispersing 0.5 g GO powder in 50 mL deionized water for 30 min. Subsequently, the above prepared few-layer $Ti_3C_2T_x$ MXene dispersion was introduced into the GO suspension, followed by additional ultrasonication for 10 min and continuous magnetic stirring for 2 h. Then, 0.5 g of mpSi powder was gradually incorporated into the mixed dispersion under vigorous magnetic stirring in an ice-water bath overnight. The resulting homogeneous dispersion was rapidly frozen in liquid nitrogen and subjected to freeze-drying at −50 °C under vacuum for 72 h to produce product that was designated as mpSi-MG.

The mpSi-MG composite was then placed in a horizontal tubular furnace and thermally treated under flowing C_2H_4/Ar atmosphere (5% v/v ethylene). The temperature was elevated to 800 °C at a heating rate of 10 °C·min^{-1} and maintained for 2 h for carbon deposition. After natural cooling to ambient temperature, the final product was collected as mpSi-MGC.

For comprehensive evaluation of electrochemical performance, three control samples were simultaneously prepared: (1) mpSi-C obtained through identical CVD carbon coating without graphene/MXene components, (2) mpSi-MG prepared by omitting the CVD carbon, and (3) mpSi-MC prepared without the graphene.

2.4 Electrode fabrication

Electrode fabrication was conducted through standardized slurry casting followed by vacuum-assisted processing. The electrode formulation consisted of active material, conductive carbon black, and sodium carboxymethyl cellulose (CMC) binder in an 8:1:1 mass ratio, which were homogenized with deionized water through high-shear mixing to achieve optimal rheological properties. The resultant slurry was doctor-bladed onto 18-μm copper current collectors under controlled gap thickness, followed by vacuum desiccation at 80 °C for 12 h to remove residual solvents. Post-drying, the composite electrodes were precision-punched into 14 mm disks using a hydraulic die cutter, yielding reproducible mass loadings of 1.4 ± 0.1 mg·cm^{-2} for electrochemical evaluation.

2.5 Materials characterization

The morphological and structural characteristics of the synthesized materials were systematically investigated using advanced characterization techniques. High-resolution field emission scanning electron microscopy (FE-SEM, Nova NanoSEM 450, FEI Company) was performed at 5 kV acceleration voltage. Microstructural evolution was further examined by transmission electron microscopy (TEM, JEM-2100F, JEOL Ltd., Japan) operating at 200 kV in bright-field mode, coupled with energy-dispersive X-ray spectroscopy (EDS, X-MaxN 80TIE250, Oxford Instruments) for elemental mapping. Crystallographic analysis was conducted on a Bragg–Brentano geometry X-ray diffractometer (X' Pert PRO MPD, PANalytical) using monochromated Cu Kα radiation (λ = 1.5406 Å) over 2θ range of 5°–90° with 0.02° step

resolution. Surface chemical states were probed by X-ray photoelectron spectroscopy (XPS, Escalab 250Xi, Thermo Scientific) employing monochromatic Al Kα excitation (1486.6 eV) with charge neutralization, while molecular vibrations were analyzed using Fourier transform infrared (FT-IR) spectroscopy (NEXUS-670, Thermo Nicolet) in transmission mode. Thermogravimetric behavior was evaluated under oxidative atmosphere (dry air) from 30–800 °C at 10 °C·min^{-1} heating ramp (STA 449C). Textural properties were quantified through N_2 physisorption at 77 K (ASAP 2020 HD, Micromeritics) following 10 h degassing at 130 °C under 10^{-3} Torr vacuum. Brunauer–Emmett–Teller (BET) surface area calculations were performed within relative pressure (P/P_0) = 0.05–0.3 range, complemented by nonlocal density functional theory (NLDFT) pore size distribution analysis. Raman spectral acquisition (LabRAM HR Evolution, HORIBA) utilized 633 nm excitation laser, calibrated using silicon reference (520.7 cm^{-1}), accumulating 3 cycles with 30 s integration time.

2.6 Electrochemical performance evaluation

The electrochemical assessments were conducted using CR2025 coin-type cells. In half-cell configurations, lithium foil served as the counter electrode, with a Celgard 2400 porous polypropylene separator and an electrolyte comprising 1 M $LiPF_6$ dissolved in ethylene carbonate (EC)/diethyl carbonate (DEC) (1:1 v/v) with 2 wt.% vinylene carbonate (VC) as an electrolyte additive. All electrochemical measurements, including galvanostatic cycling (0.01–2.0 V vs. Li^+/Li) and galvanostatic intermittent titration technique (GITT) analysis, were performed on a Neware battery testing system (Shenzhen Neware Co., Ltd., China). The specific capacity was determined based on the active mass of the silicon component in the working electrode. Electrochemical impedance spectroscopy (EIS) measurements were acquired using a CHI660E electrochemical workstation over a frequency range of 0.01 to 100 kHz. All tests were conducted under controlled ambient conditions (25 ± 2 °C) unless otherwise specified. In addition, in order to improve the initial Coulombic efficiency (ICE) of the prepared material electrode, pre-lithiation treatment was carried out. This was achieved by bringing the electrode coated with active material into full contact with lithium foil in the presence of electrolyte for 25 min.

Full cells were assembled in 2025-type coin configurations employing pre-lithiated mpSi-MGC composite anodes paired with commercial $LiNi_{0.8}Co_{0.1}Mn_{0.1}O_2$ (NCM811) cathodes, maintaining a capacity balancing (N/P ratio) of 1.1. The cathode slurry was formulated by homogenizing NCM811 active material, conductive carbon black, and polyvinylidene fluoride (PVDF) binder at an 8:1:1 mass ratio in N-methyl-2-pyrrolidone (NMP) solvent, followed by doctor-blade coating onto aluminum foil, vacuum drying at 80 °C for 12 h, and precision punching into 12 mm disks. Full-cell evaluations involved galvanostatic charge/discharge cycling between 3.0–4.3 V, with specific capacity normalized to the cathode active material mass.

3 Results and discussion

The fabrication procedure of the mpSi-MGC composite is schematically illustrated in Fig. 1(a). Initially, micro-sized porous silicon (mpSi) was obtained through selective etching of a commercial $Al_{60}Si_{40}$ alloy using a hydrochloric acid aqueous solution with optimized concentration. Subsequently, the prepared mpSi was uniformly dispersed into a mixed colloidal suspension containing few-layer $Ti_3C_2T_x$ MXene and exfoliated GO nanosheets. Hydrogen bonds are formed between the hydroxyl groups on the MXene surface and the carboxyl groups on the GO surface, enabling the assembly of the two components. Concurrently, Ti–O–C bonds (titanium-oxygen-carbon bonds) and Ti–O–Ti bonds (titanium-oxygen-titanium bonds) are generated, which significantly enhance the mechanical strength of the MXene/GO hybrid coating. In addition, the incorporation of freeze-drying technology facilitates the formation of a three-dimensional (3D) framework structure. In the subsequent stage, the dense chemical vapor deposition (CVD) carbon coating deposited on the exterior of the framework further improves the mechanical strength and electrical conductivity of the material. Eventually, a hierarchical composite anode material with an MXene/rGO hybrid wrapping layer and a CVD carbon coating structure is formed, which is designated as mpSi-MGC.

Figure S1 in the Electronic Supplementary Material (ESM) presents the X-ray diffraction (XRD) pattern and SEM image of pristine Ti_3AlC_2 MAX phase, confirming its high phase purity with negligible two-dimensional layered characteristics. After chemical etching using the HCl-LiF system (Fig. S2 in the ESM), the initially delaminated $Ti_3C_2T_x$ MXene exhibited distinct stacked lamellar structures. To obtain few-layer $Ti_3C_2T_x$ nanosheets, controlled ultrasonication combined with differential centrifugation was systematically implemented to prepare the colloidal suspension. The structural evolution during exfoliation is evidenced by XRD patterns in Fig. S3(a) in the ESM, where the characteristic (002) diffraction peak shifted significantly from 9.8° to 6.7°, unambiguously demonstrating interlayer spacing expansion through successful delamination. Notably, the acquired dark green coloration of the few-layer $Ti_3C_2T_x$ dispersion (Fig. S3(b) in the ESM) indicates modified optical absorption properties due to dimensional reduction, providing supplementary evidence for effective exfoliation.

The morphology of mpSi-MGC was comprehensively characterized by SEM (Figs. 1(b) and 1(c) and Figs. S4(a) and S4(b) in the ESM), revealing mpSi particles tightly encapsulated within the hybrid matrix composed of few-layer $Ti_3C_2T_x$ and rGO nanosheets. The morphology of mpSi-MGC was comprehensively characterized by SEM (Figs. 1(d) and 1(e)) further elucidates the hierarchical architecture, including the conformal CVD carbon coating and homogeneous Si distribution. Comparative morphological studies with control samples (mpSi-C in Fig. S5 in the ESM, mpSi-MG in Fig. S6 in the ESM, and mpSi-MC in Fig. S7 in the ESM) demonstrate distinct structural differences. High-resolution TEM (HRTEM) images (Figs. 1(f)–1(i)) distinctly resolve lattice fringes corresponding to (200) planes of $Ti_3C_2T_x$, (220) planes of crystalline Si, and (002) planes of rGO, confirming the successful integration of all components. Elemental mapping analysis (Figs. 1(j)–1(n)) reveals uniform distribution of Si, C, and Ti elements, along with residual F species originating from the terminal groups (–O and –F) of $Ti_3C_2T_x$ MXene. As will be discussed later, these fluorine moieties are anticipated to facilitate the formation of LiF-enriched SEI layers during electrochemical cycling.

Figure 2(a) presents the XRD patterns of mpSi-MGC and mpSi-MG samples. The diffraction peaks corresponding to Si align well with the cubic phase of crystalline silicon (JCPDS No. 27-1402).

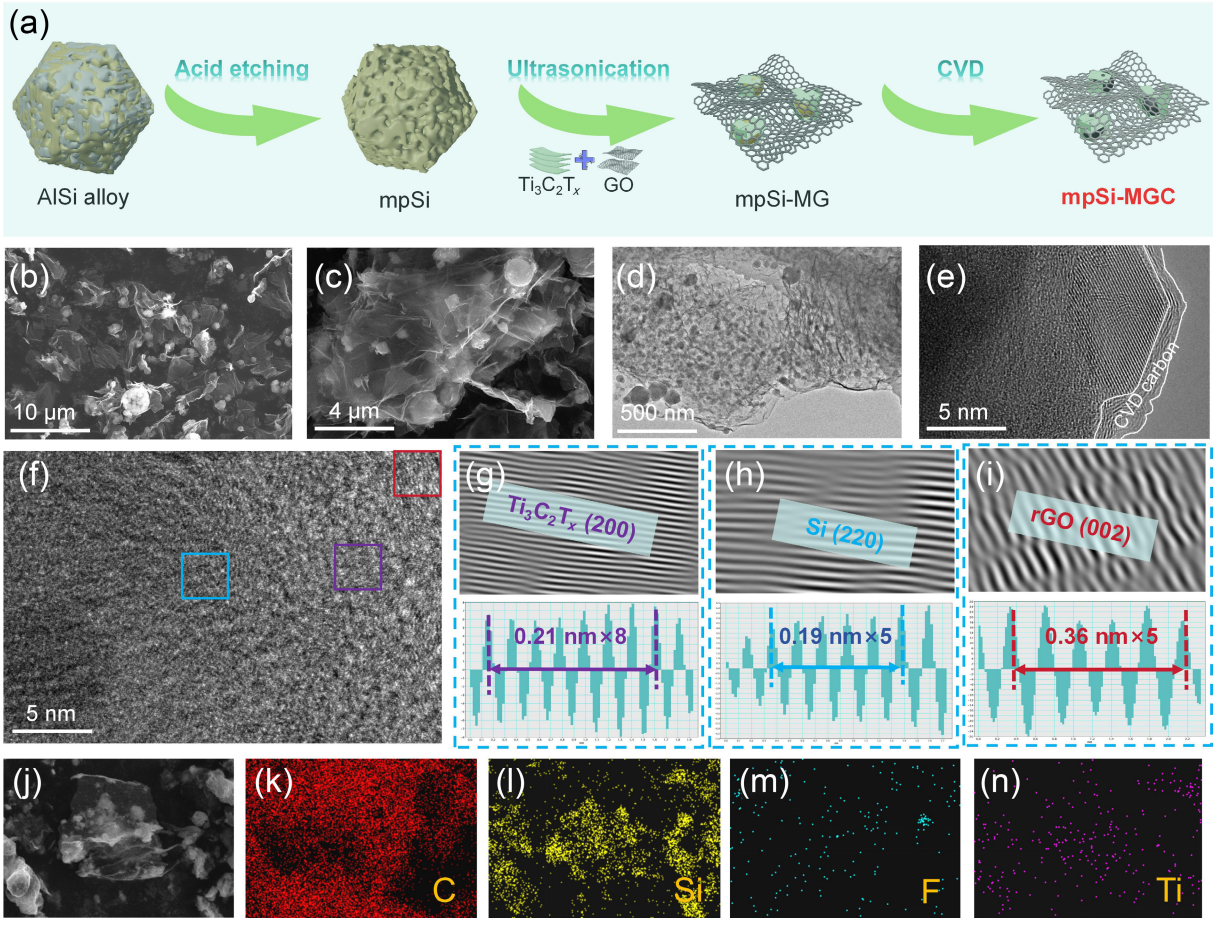

Figure 1 (a) Schematic diagram of the preparation process of the mpSi sample. ((b) and (c)) SEM images of the mpSi sample at different magnifications. ((d) and (e)) TEM images of the mpSi sample at different magnifications. ((f)–(i)) HRTEM images of the mpSi sample and the lattice fringe spacing of the corresponding components. ((j)–(n)) SEM image of the mpSi sample and the corresponding elemental distribution.

Notably, the characteristic peak of GO at 2θ = 26° undergoes a distinct shift to 2θ = 11° after CVD treatment, corresponding to the rGO signature. This transformation confirms the thermal reduction of GO to rGO during CVD processing, where the removal of oxygen-containing functional groups results in an enlarged interlayer spacing [35, 36]. The Raman spectrum of mpSi-MGC (Fig. 2(b)) exhibits two prominent scattering peaks at 503 and 946 cm^{-1}, attributed to crystalline silicon. Additionally, the D-band (1350 cm^{-1}) and G-band (1586 cm^{-1}) of carbon species display an intensity ratio (I_D/I_G) of 0.832, indicative of a high graphitization degree in the carbon matrix. This enhanced graphitic ordering contributes significantly to improving the overall electrical conductivity of the composite electrode [37]. FT-IR analysis of mpSi-MGC (Fig. 2(c)) reveals absorption bands at ~ 1077 and 471 cm^{-1}, assigned to the asymmetric stretching and bending vibrations of Si–O–Si bonds, respectively [38, 39]. Peaks observed at 3434 and 1631 cm^{-1} correspond to O–H stretching vibrations and C=O stretching modes, while the peak at ~ 700 cm^{-1} is attributed to Ti–F bonds, respectively [40]. These findings collectively demonstrate the formation of robust chemical bonding between Si and $Ti_3C_2T_x$ MXene.

XPS spectra (Figs. 2(d)–2(f) and Fig. S8 in the ESM) were employed to investigate the elemental composition and surface electronic states of mpSi-MGC. The survey spectrum (Fig. S8(a) in the ESM) confirms the presence of Si, O, C, and Ti. High-resolution O 1s spectrum (Fig. 2(d)) deconvolutes into four components at 533.1, 531.8, 530.6, and 529.2 eV, corresponding to H–O, Si–O, C–Ti–O_x, and Ti–O bonds, respectively [41–44]. The dominance of Si^{4+} (103.8 eV) over Si^0 (99.3 eV) in the unetched Si 2p spectra (Fig. 2(e)) suggests surface oxidation of mpSi due to interactions with oxygen-rich functional groups on GO and MXene. Prolonged etching gradually reveals lower oxidation states (Si^0, Si^{2+}, and Si^{3+}), confirming that oxidation is confined to the surface layer. Further evidence of chemical bonding between mpSi, GO, and MXene is provided by the Ti 2p and C 1s spectra (Fig. 2(f) and Fig. S8(b) in the ESM).

Thermogravimetric analysis (TGA) (Fig. 2(g)) reveals a 37.1% weight loss for mpSi-MGC between 350–650 °C, compared to 16.8% for mpSi-MC, indicating an estimated rGO content of ~ 20.3%. N_2 adsorption–desorption isotherms (Fig. 2(h)) demonstrate that the hybrid coating of rGO/MXene and CVD carbon coating encapsulation reduces the specific surface area of mpSi-MGC to 18.2 $m^2 \cdot g^{-1}$, substantially lower than that of pristine mpSi (~ 40 $m^2 \cdot g^{-1}$) [45]. Nevertheless, the preserved mesoporous structure with an average pore diameter of 20.1 nm (Fig. 2(i)) provides critical buffer space to accommodate volume expansion of active materials during electrochemical cycling.

To systematically evaluate the application prospects of mpSi-MGC as an advanced Si-based anode material for LIBs, we conducted a series of electrochemical performance tests. Figure 3(a)

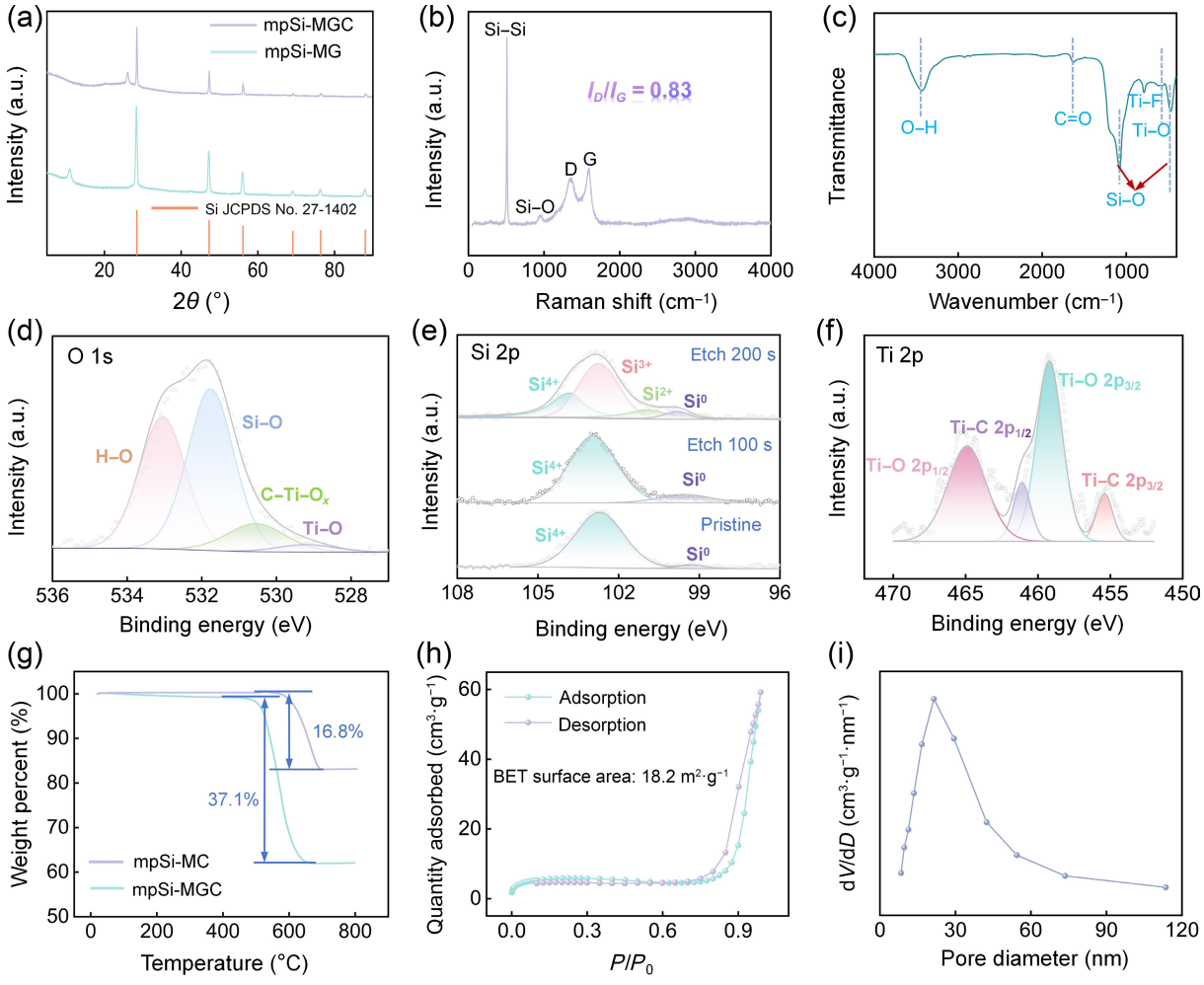

Figure 2 (a) XRD patterns of mpSi-MG and mpSi-MGC. (b) Raman spectrum of the mpSi-MGC. (c) FT-IR spectrum of the mpSi-MGC. ((d)–(f)) XPS spectra of the mpSi-MGC for various elements: (d) O 1s, (e) Si 2p at different etching time, and (f) Ti 2p. (g) TGA curves of mpSi-MC and mpSi-MGC. (h) The N_2 isothermal adsorption–desorption curves of the mpSi-MGC sample at 77 K. (i) The corresponding pore size distribution.

displays the first three cyclic voltammetry (CV) curves of the mpSi-MGC electrode within a voltage window of 0–3.0 V at a scan rate of 0.2 mV·s^{-1}. During the initial lithiation process, two irreversible cathodic peaks are clearly observed. The broad peak spanning 0.7–1.9 V corresponds to the formation of the SEI layer [46, 47]. In the delithiation process, two anodic peaks at 0.34 and 0.49 V are identified, reflecting the phase transition from Li–Si alloy to amorphous Si [48]. The progressive enhancement of delithiation peak currents in subsequent cycles, driven by the activation of active materials, confirms the reversible nature of Li^+ storage and extraction. These CV results unambiguously demonstrate the reversible electrochemical interaction between Li^+ and the mpSi-MGC electrode. Figure 3(b) illustrates the galvanostatic charge/discharge profiles of the mpSi-MGC electrode at a current density of 0.2 A·g^{-1}. The minimal variation in voltage plateau profiles and curve shapes from the 1st to the 100th cycle underscores the electrode's exceptional electrochemical stability.

A comparative analysis of the initial charge/discharge curves before and after pre-lithiation is presented in Fig. 3(c). The pristine mpSi-MGC electrode exhibits initial discharge and charge capacities of 2410 and 1535 mAh·g^{-1}, respectively, yielding an ICE of 63.7%. Following pre-lithiation, the corresponding values shift to 1500 and 1438 mAh·g^{-1}, with ICE significantly enhanced to 95.9%. This demonstrates that a straightforward contact pre-lithiation strategy effectively optimizes the ICE of mpSi-MGC. Figure 3(d) highlights the rate capabilities of mpSi-MGC compared to control electrodes (mpSi-MC and mpSi-C). The mpSi-MGC electrode exhibits superior rate performance, delivering a reversible capacity of 852 mAh·g^{-1} at 3 A·g^{-1} and recovering to 1364 mAh·g^{-1} upon returning to 0.2 A·g^{-1}, indicative of robust structural integrity and rapid ion/electron transport kinetics.

Long-term cycling stability at varying current densities is depicted in Figs. 3(e) and 3(f) and Fig. S9 in the ESM. The mpSi-MGC electrode achieves the highest reversible capacity and cycling durability, retaining 1800 mAh·g^{-1} (69.7% capacity retention) after 100 cycles at 0.2 A·g^{-1}. In stark contrast, mpSi-MC and mpSi-C electrodes suffer severe capacity degradation, retaining only 495 and 64 mAh·g^{-1}, respectively. This performance superiority confirms that the hybrid encapsulation with few layer $Ti_3C_2T_x$ and rGO not only enhances bulk conductivity but also reinforces structural stability and reversible capacity during prolonged cycling [49]. The supplementary CVD carbon coating further contributes to performance optimization, as evidenced by the inferior capacity retention and rate capability of the carbon-free mpSi-MG electrode (Fig. S9 in the ESM). These findings collectively reveal synergistic effects among $Ti_3C_2T_x$, rGO, and CVD carbon coating in enhancing electrode performance.

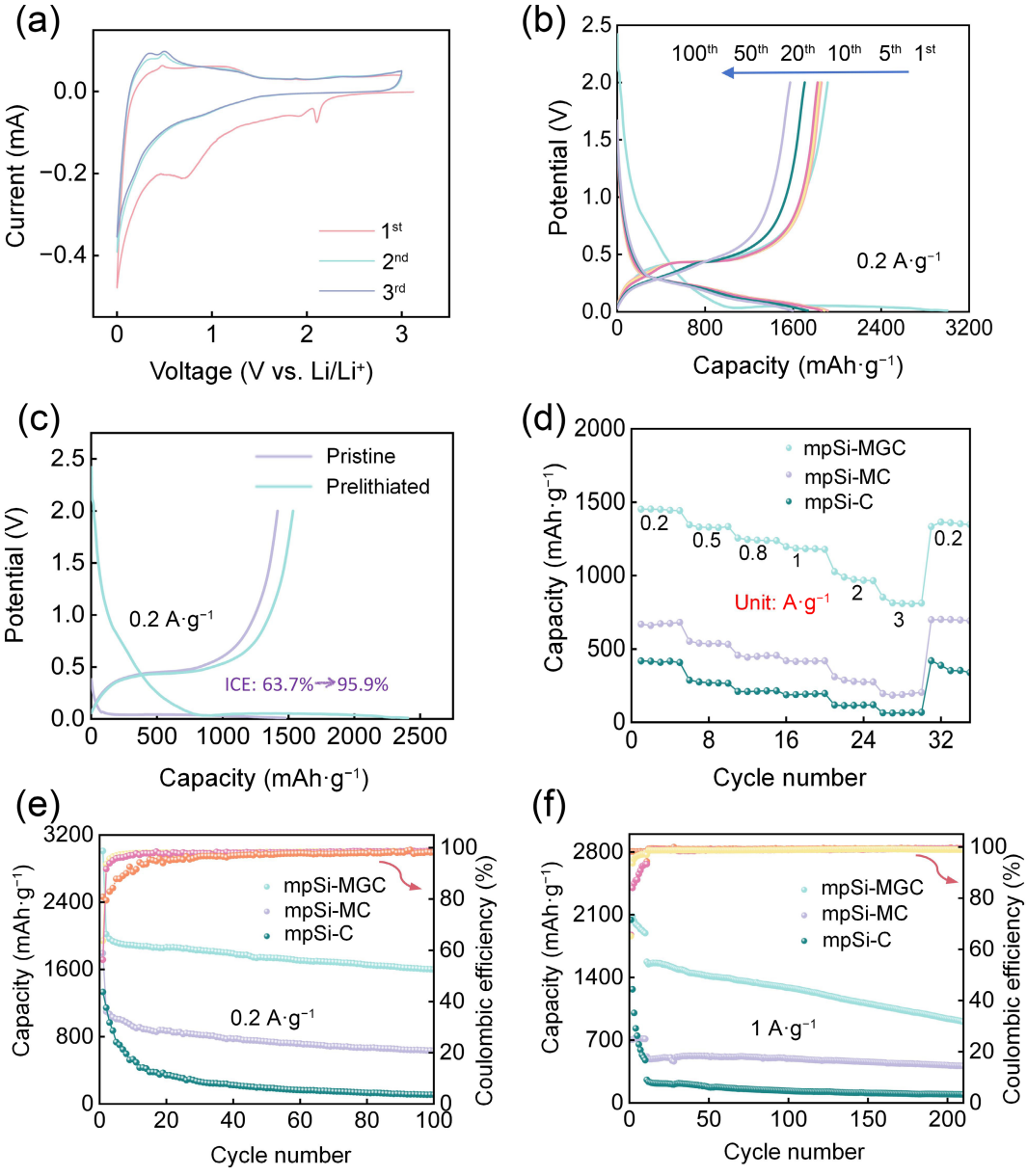

Figure 3 (a) CV curves of the first three cycles of the mpSi-MGC electrode. (b) Voltage profiles of the mpSi-MGC electrode at different cycle numbers under a current density of 0.2 A·g^{-1}. (c) First charge–discharge curves of the mpSi-MGC electrode before and after prelithiation. (d) Rate capability of the mpSi-C, mpSi-MC, and mpSi-MGC electrodes. ((e) and (f)) Long-term cycling stability of mpSi-C, mpSi-MC, and mpSi-MGC electrodes at different current densities: (e) 0.2 A·g^{-1} and (f) 1 A·g^{-1}.

To probe volume evolution during cycling, post-cycled electrodes were analyzed via surface and cross-sectional SEM (Fig. S10 in the ESM). The mpSi-MGC electrode exhibits a moderate volume expansion of 17.3% after 50 cycles at 0.3 A·g^{-1}, with a crack-free surface morphology. Conversely, mpSi-MC and mpSi-C electrodes undergo severe expansion (126.9% and 192.3%, respectively) accompanied by extensive surface cracking. Furthermore, the elemental mapping images of the mpSi-MGC electrode surface after cycling (Fig. S11 in the ESM) also reveal that F, P, and O elements are uniformly distributed within the Si matrix. These results unequivocally validate that hybrid surface encapsulation effectively mitigates volume expansion during lithiation/delithiation processes.

To systematically elucidate the mechanistic enhancement of Li^+ and e^- transport kinetics in mpSi through the synergistic incorporation of few-layer $Ti_3C_2T_x$ MXene, rGO, and CVD carbon coating, we conducted a series of validation experiments. First, comparative XPS analysis was performed on mpSi-MGC and mpSi-C electrodes after 20 charge/discharge cycles. High-resolution F 1s spectra (Fig. 4(a)) reveal a substantial increase in LiF content within the mpSi-MGC electrode (44.59%) compared to the $Ti_3C_2T_x$/rGO-free mpSi-C counterpart (15.12%) (Fig. 4(b)). This LiF enrichment was further corroborated by Li 1s spectral analysis (Figs. 4(c) and 4(d)), demonstrating that fluorine-containing functional groups in $Ti_3C_2T_x$ effectively facilitate the formation of a LiF-rich SEI layer, thereby accelerating Li^+ transport kinetics. A LiF-rich SEI layer can provide more and faster channels for Li^+ transport, thereby accelerating lithium-ion diffusion and improving rate capability. Simultaneously, the high mechanical strength of LiF effectively enhances the mechanical robustness of the SEI layer, preventing its repeated fracture and reformation. This significantly reduces the continuous consumption of active lithium and electrolyte, leading to a remarkable improvement in the cycling stability of the battery.

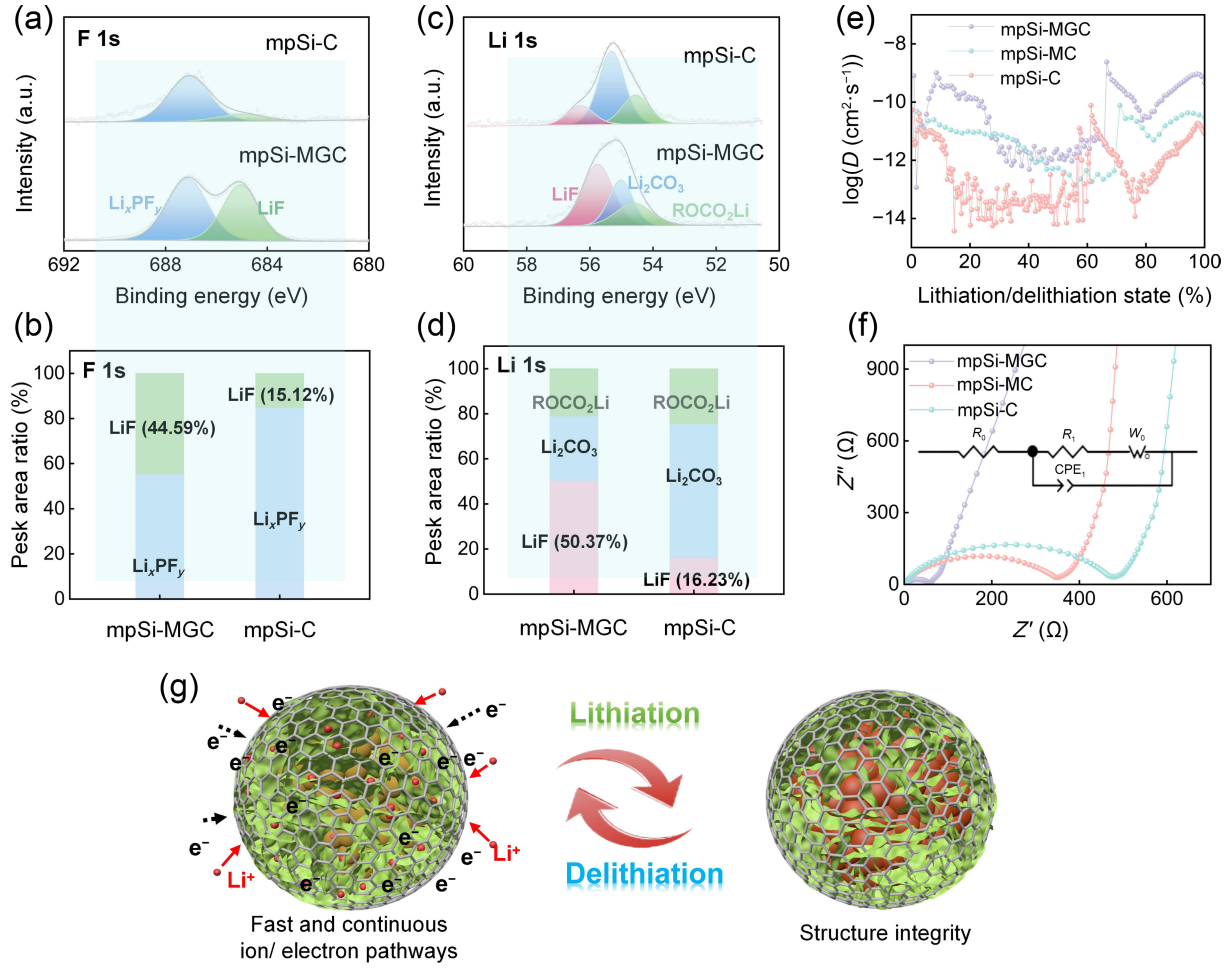

Figure 4 (a) The F 1s XPS spectra of mpSi-C and mpSi-MGC electrodes after 20 cycles and (b) the corresponding relative content of LiF calculated from the integrated peak areas. (c) The Li 1s XPS spectra of the two electrodes. (d) The corresponding relative content of LiF. (e) GITT curves of the mpSi-C, mpSi-MC, and mpSi-MGC electrodes. (f) EIS of the pristine mpSi-C, mpSi-MC, and mpSi-MGC electrodes and the corresponding equivalent circuit diagrams. (g) Schematic diagram of the structural changes of the mpSi-MGC electrode during the lithiation and delithiation processes and the optimization of the ion/electron transport paths.

To quantitatively verify this mechanism, we employed GITT at 0.05 mA·g^{-1} (Fig. S12 in the ESM) to analyze relaxation behavior and calculate Li^+ diffusion coefficients (D_{Li^+}) during cycling. As shown in $Ti_3C_2T_x$ in Fig. 4(e), the mpSi-MGC electrode exhibits superior D_{Li^+} values ranging from 10^{-9} to 10^{-12} cm^2·s^{-1}, significantly higher than those of mpSi-MC (10^{-10}–10^{-13} cm^2·s^{-1}) and mpSi-C (10^{-10}–10^{-14} cm^2·s^{-1}) electrodes. These results, combined with post-cycling XPS analysis, conclusively demonstrate the critical role of in enhancing Li^+ diffusion kinetics.

To evaluate the hybrid encapsulation's impact on electrode conductivity, we conducted EIS before and after cycling. The Nyquist plots (Fig. 4(f) and Fig. S13 in the ESM) with corresponding equivalent circuit models (inset, Fig. 4(f)) reveal significantly lower charge transfer resistance (R_{ct}) for mpSi-MGC compared to control electrodes. This improvement stems from the three-dimensional conductive network formed by $Ti_3C_2T_x$/rGO/CVD-carbon hybridization. Notably, Fig. S13 in the ESM demonstrates progressive R_{ct} reduction with cycling, attributable to enhanced electrolyte infiltration into electrode pores and optimized electrode/electrolyte interfacial contact [50].

The synergistic combination of fluorine-functionalized $Ti_3C_2T_x$ rGO and CVD carbon coating establishes continuous pathways for rapid electron/ion transport while maintaining electrode structural integrity (Fig. 4(g)). This multifunctional architecture addresses critical challenges in Si-based anodes by simultaneously enhancing ionic conductivity through LiF-rich SEI formation and electronic conductivity via 3D percolation networks.

To elucidate the Li storage mechanisms of the mpSi-MGC electrode, comparative CV analyses were systematically conducted on mpSi-MGC, mpSi-MC, and mpSi-C electrodes across scan rates of 0.2–0.7 mV·s^{-1} (Fig. 5(a)). The electrochemical kinetics governing charge storage behavior can be quantitatively differentiated through the power-law relationship between current response (i) and scan rate (v)

$$i = av^b \quad (1)$$

$$\log i = b\log v + \log a \quad (2)$$

where a is a proportional constant. b-values derived from linear regression analysis (Fig. 5(b)) provide critical mechanistic insights. The calculated b-values of 0.56 (Peak 1) and 0.62 (Peak 2) for mpSi-MGC indicate a hybrid charge storage mechanism combining diffusion-controlled and capacitive-dominated processes [51]. The capacitive contribution is attributed to synergistic effects from oxygen-functionalized $Ti_3C_2T_x$ surfaces, rGO integration, and CVD

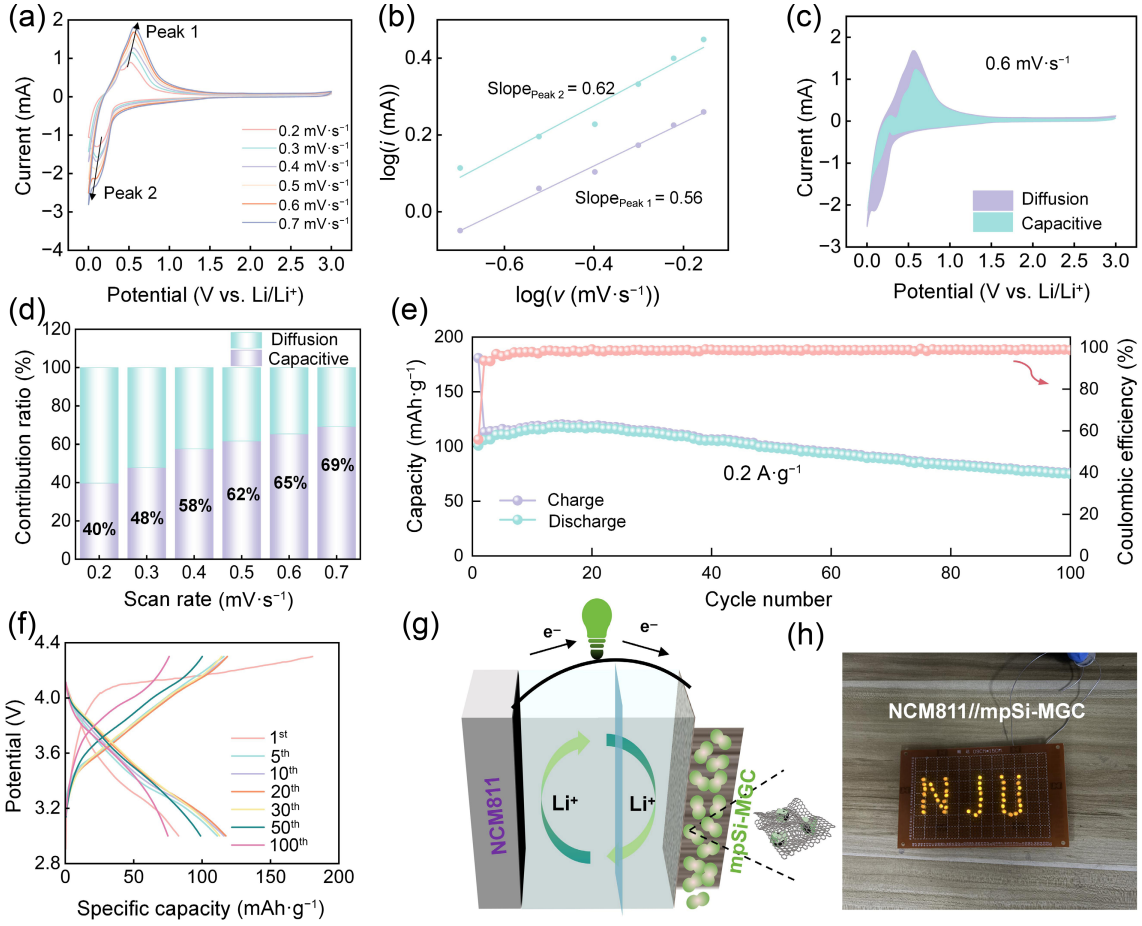

Figure 5 (a) CV curves of the mpSi-MGC electrode at different scanning rates. (b) log*i* against log*v* at assigned peaks of mpSi-MGC. (c) The detailed pseudocapacitive contribution at 0.6 mV·s^{-1} for mpSi-MGC. (d) The specific proportions of pseudocapacitive control and diffusion control contributions to the battery capacity of the mpSi-MGC electrode at different scanning rates. (e) Cycling stability of the NCM811//mpSi-MGC full battery at a current density of 0.2 A·g^{-1}. (f) Voltage profiles of the NCM811//mpSi-MGC full battery at different cycle numbers. (g) The NCM811//mpSi-MGC full battery lights up 44 LED bulbs simultaneously. (h) The configuration of the NCM811//mpSi-MGC full battery.

carbon coating matrix. Quantitative deconvolution of capacitive contributions (Figs. 5(c) and 5(d) and Figs. S14(a)–S14(e) in the ESM) reveals a 65% capacitive dominance at 0.6 mV·s^{-1}, with progressive enhancement at elevated scan rates. Notably, mpSi-MC electrodes exhibit analogous dual-mode behavior (Figs. S15(a)–S15(h) in the ESM), primarily governed by $Ti_3C_2T_x$ and CVD-carbon interfaces. Capacitive behavior enables rapid charge transfer, allowing the electrode to maintain excellent responsiveness even at high scan rates, while diffusion processes ensure high specific capacity. The synergistic interaction between these two mechanisms achieves an optimal balance between rate capability and capacity retention, enabling the mpSi-MGC material to deliver stable performance across current densities ranging from 0.2 to 1 A·g^{-1}.

To evaluate practical viability, full-cells were assembled using NCM811 cathodes (cell configuration: Fig. 5(g)). The mpSi-MGC//NCM811 system demonstrates exceptional cyclability, retaining 74.4% capacity (75 mAh·g^{-1}) after 100 cycles at 0.2 A·g^{-1} (Fig. 5(e)). Well-defined charge/discharge plateaus persist throughout cycling (Fig. 5(f)), confirming stable electrochemical kinetics. Practical applicability is further evidenced by successful power delivery to a 44-light-emitting diode (LED) array (Fig. 5(h)), highlighting operational stability under realistic load conditions.

4 Conclusions

In summary, this study successfully fabricated a mpSi-MGC through a synergistic combination of self-assembly techniques and CVD processes. The hierarchical architecture features few-layer $Ti_3C_2T_x$ MXene, rGO, and CVD carbon layers forming a multi-confinement encapsulation system. This sophisticated structural design not only endows the mpSi core with exceptional mechanical robustness but also significantly optimizes both electronic and ionic transport kinetics. *Ex situ* characterization systematically revealed that the enhanced Li^+ diffusion coefficients in the mpSi-MGC electrode originate from F-functionalized groups within the $Ti_3C_2T_x$ matrix. These fluorinated moieties substantially facilitate the formation of a LiF-rich SEI layer, while the exterior CVD-carbon coating on the 2D $Ti_3C_2T_x$/rGO assembly further reinforces structural integrity through secondary confinement effects. The resultant multi-confinement architecture demonstrates outstanding electrochemical performance: delivering a remarkable reversible capacity of 1800 mAh·g^{-1} at 0.2 A·g^{-1}, maintaining 992 mAh·g^{-1} after 200 cycles at 1.0 A·g^{-1}, and exhibiting superior rate capability with 818 mAh·g^{-1} at 3 A·g^{-1}. This multi-scale confinement strategy presents profound implications for addressing the critical challenges of volumetric expansion in mpSi anodes while simultaneously enhancing Li^+/e^- conductivity. The proposed structural paradigm

offers novel conceptual guidance for developing high-energy-density LIBs, particularly in advancing micron-scale Si anode technologies through rational interface engineering and multidimensional transport pathway optimization.

Electronic Supplementary Material: Supplementary material (SEM images, XRD patterns, HRTEM images, digital photograph, cycling performance, XPS spectra, GITT curves, Nyquist plots, and CV curves) is available in the online version of this article at https://doi.org/10.26599/NR.2025.94908024.

Data availability

All data needed to support the conclusions in the paper are presented in the manuscript and the Electronic Supplementary Material. Additional data related to this paper may be requested from the corresponding author upon request.

Acknowledgements

The authors gratefully acknowledge financial support from the National Natural Science Foundation of China (Nos. 52202309, U25A20628, 22561160129, 22479074, and 22475096), Major Project for Basic and Natural Sciences Research of Jiangsu Provincial Colleges and Universities (No. 25KJA150006), Yancheng Science and Technology Program—Science and Technology Cooperation Project with Hong Kong, Macao, and Taiwan (No. Ycgh2025008), Qing Lan Project of Jiangsu Province, the Open Program of State Key Laboratory of Coordination Chemistry (No. SKLCC2308), Postgraduate Scientific Research Innovation Program of Jiangsu Province (No. KYCX25_3879), the Equipment Pre-Research and Ministry of Education Joint Fund (No. 8091B02052407), the Scientific and Technological Achievements Transformation Special Fund of Jiangsu Province (No. BA2023037), the Natural Science Foundation of Jiangsu Province (Nos. BK20240400 and BK20241236), the International Collaboration Research Program of Nanjing City (Nos. 202201007 and 2022SX00000955), the Gusu Leading Talent Program of Scientific and Technological Innovation and Entrepreneurship of Wujiang District in Suzhou City (No. ZXL2021273), the Chenzhou National Sustainable Development Agenda Innovation Demonstration Zone Provincial Special Project (No. 2023sfq11), the Technology Innovation Team of Yancheng Polytechnic College (No. YGKJ202503), the Fundamental Research Program Key Project of Jiangsu Province (No. BK20253008), the Science and Technology Major Project of Jiangsu Province (No. BG2024013), the Academic Degree and Postgraduate Education Reforming Project of Jiangsu Province (No. JGKT24_C001), the Key Core Technology Open Competition Project of Suzhou City (No. SYG2024122), and the Open Research Fund of Suzhou Laboratory (No. SZLAB-1308-2024-TS005).

Declaration of competing interest

All the contributing authors report no conflict of interests in this work.

Author contribution statement

L. S.: Data curation, project administration, funding acquisition, experimental design, writing manuscript. L. J. W.: Data curation. T. Q. W.: Data curation. Y. Y. L.: Data curation. Y. J. Q.: Data curation. X. T. L.: Data curation. M. Q.: Validation. Z. J.: Project administration, funding acquisition. All the authors have approved the final manuscript.

Use of AI statement

None.

References

[1] Ahad, S. A.; Kennedy, T.; Geaney, H. Si nanowires: From model system to practical Li-ion anode material and beyond. *ACS Energy Lett.* **2024**, *9*, 1548–1561.

[2] Sun, L.; Liu, Y.; Wang, L. J.; Jin, Z. Advances and future prospects of micro-silicon anodes for high-energy-density lithium-ion batteries: A comprehensive review. *Adv. Funct. Mater.* **2024**, *34*, 2403032.

[3] Yang, Y. F.; Biswas, S.; Xu, R.; Xiao, X.; Xu, X.; Zhang, P.; Gong, H. X.; Zheng, X. L.; Peng, Y. C.; Li, J. Y. et al. Capacity recovery by transient voltage pulse in silicon-anode batteries. *Science* **2024**, *386*, 322–327.

[4] Kim, N.; Kim, Y.; Sung, J.; Cho, J. Issues impeding the commercialization of laboratory innovations for energy-dense Si-containing lithium-ion batteries. *Nat. Energy* **2023**, *8*, 921–933.

[5] Li, Q.; Ruan, J. F.; Weng, S. T.; Zhang, X.; Hu, J. M.; Li, H.; Sun, D. L.; Wang, X. F.; Fang, F.; Wang, F. Interphasial pre-lithiation and reinforcement of micro-Si anode through fluorine-free electrolytes. *Angew. Chem., Int. Ed.* **2023**, *62*, e202310297.

[6] Wang, H. L.; Chao, Y. F.; Li, J. Z.; Qi, Q.; Lu, J. F.; Yan, P. F.; Nie, Y. Y.; Wang, L.; Chen, J. F.; Cui, X. W. What is the real origin of single-walled carbon nanotubes for the performance enhancement of Si-based anodes? *J. Am. Chem. Soc.* **2024**, *146*, 17041–17053.

[7] Zhang, M. Y.; Liang, N. W.; Hao, D.; Chen, Z. X.; Zhang, F.; Yin, J.; Yang, Y. H.; Yang, L.-S. Recent advances of SiO_x-based anodes for sustainable lithium-ion batteries. *Nano Res. Energy* **2023**, *2*, e9120077

[8] Jia, P. S.; Guo, J. P.; Li, Q.; Liu, Y. N.; Zheng, Y.; Guo, Y.; Huang, Y. K.; Shen, Y. Y.; Long, L. F.; Zhang, H. B. et al. Revisiting the kinetics enhancement strategies of Si anodes through deconstructing particle-interface-electrode integration. *Energy Environ. Sci.* **2025**, *18*, 2720–2746.

[9] Sun, L.; Liu, Y. X.; Shao, R.; Wu, J.; Jiang, R. Y.; Jin, Z. Recent progress and future perspective on practical silicon anode-based lithium ion batteries. *Energy Storage Mater.* **2022**, *46*, 482–502.

[10] Sun, L.; Liu, Y.; Wang, L. Y.; Chen, Z. D.; Jin, Z. Stabilizing porous micro-sized silicon anodes via construction of tough composite interface networks for high-energy-density lithium-ion batteries. *Nano Res.* **2024**, *17*, 9737–9745.

[11] Zhang, C. Z.; Wang, F.; Han, J.; Bai, S.; Tan, J.; Liu, J. S.; Li, F. Challenges and recent progress on silicon-based anode materials for next-generation lithium-ion batteries. *Small Struct.* **2021**, *2*, 2100009.

[12] Saana Amiinu, I.; Imtiaz, S.; Geaney, H.; Kennedy, T.; Kapuria, N.; Singh, S.; Ryan, K. M. A thin Si nanowire network anode for high volumetric capacity and long-life lithium-ion batteries. *J. Energy Chem.* **2023**, *81*, 20–27.

[13] Sonia, F. J.; Haider, G.; Ghosh, S.; Müller, M.; Volochanskyi, O.; Bouša, M.; Plšek, J.; Kamruddin, M.; Fejfar, A.; Kalbáč, M. et al. Interface and morphology engineered amorphous Si for ultrafast electrochemical lithium storage. *Small* **2024**, *20*, 2311250.

[14] Mu, X.; Xu, X. T.; Xu, H. B.; Huang, T.; Yu, A. S. Ultrastable monodisperse resin-based spherical Si–C materials with micropore confined growth of silicon nanoclusters for lithium-ion battery anodes. *Adv. Funct. Mater.*, in press, DOI: 10.1002/adfm.202504545.

[15] Sun, L.; Wang, X.; Liu, Y.; Xu, H. N.; Wang, H. Y.; Lu, Y. Y.; Jin, Z. Facile redox synthesis and surface engineering of porous silicon from

zintl compound for high-performance lithium ion battery anodes. *ACS Appl. Mater. Interfaces* **2024**, *16*, 52349–52357.

[16] Xue, X.; Lou, B.; Wu, C. C.; Pang, W. W.; Zhang, J. C.; Shi, N.; Men, Z. W.; Wen, F. S.; Yang, X. J.; Wu, J. et al. The impact of carbon material microstructure on Li-ion storage behaviors of Si in Si/C anodes. *Chem. Eng. J.* **2024**, *488*, 150936.

[17] Wang, J. W.; Bai, Z. W.; Zhao, Z. J.; Zheng, G. P.; Cheng, J. Y.; Chen, G. H. Electron/ion-conductive and flexible dual-functional copolymer enabled by EDOT and h_2PDMS for optimized Li-ion batteries. *Nano Res. Energy* **2025**, *4*, e9120133

[18] Li, M.; Li, H.; Jiang, Q. T.; Wang, J. J.; Cao, G. Q.; Duan, R. X.; Li, J.; Bai, M. X.; Zuo, J. X.; Yang, Z. H. et al. Inner helmholtz plane constructing LiF-rich solid electrolyte interphase of silicon anodes. *Nano Energy* **2025**, *139*, 110951.

[19] Sun, J. R.; Chen, G. D.; Wang, B.; Li, J. D.; Xu, G. J.; Wu, T. Y.; Tang, Y. F.; Dong, S. M.; Huang, J. Y.; Cui, G. L. Lithium hydride in the solid electrolyte interphase of lithium-ion batteries as a pulverization accelerator of silicon. *Angew. Chem., Int. Ed.* **2024**, *63*, e202406198.

[20] Yang, Y. Z.; Wang, J.; Li, Z. L.; Yang, Z.; Wang, B.; Zhao, H. L. Constructing LiF-dominated interphases with polymer interwoven outer layer enables long-term cycling of Si anodes. *ACS Nano* **2024**, *18*, 7666–7676.

[21] He, Z. Y.; Xiao, Z. X.; Yue, H. J.; Jiang, Y. X.; Zhao, M. Y.; Zhu, Y. K.; Yu, C. H.; Zhu, Z. X.; Lu, F.; Jiang, H. R. et al. Single-walled carbon nanotube film as an efficient conductive network for Si-based anodes. *Adv. Funct. Mater.* **2023**, *33*, 2300094.

[22] Kang, Y. J.; Lin, D. L.; Liu, B. X.; Dong, N. X.; Zhao, Z.; Tian, G. F.; Qi, S. L.; Wu, D. Z. *In situ* engineering of a 3D branched polyimide/silver interface layer with dual ion-electron conductivity for superior structural integrity and long-cycle stability of silicon anodes. *Adv. Funct. Mater.*, in press, DOI: 10.1002/adfm.202504861.

[23] Zhou, J.; Zhou, L.; Yang, L. S.; Chen, T.; Li, J. Q.; Pan, H.; Yang, Y. H.; Wang, Z. C. Carbon free silicon/polyaniline hybrid anodes with 3D conductive structures for superior lithium-ion batteries. *Chem. Commun.* **2020**, *56*, 2328–2331.

[24] Man, Q. Y.; An, Y. L.; Liu, C. K.; Shen, H. T.; Xiong, S. L.; Feng, J. K. Interfacial design of silicon/carbon anodes for rechargeable batteries: A review. *J. Energy Chem.* **2023**, *76*, 576–600.

[25] Zhang, W.; Gui, S. W.; Li, W. M.; Tu, S. B.; Li, G. C.; Zhang, Y.; Sun, Y. M.; Xie, J. Y.; Zhou, H. M.; Yang, H. Functionally gradient silicon/graphite composite electrodes enabling stable cycling and high capacity for lithium-ion batteries. *ACS Appl. Mater. Interfaces* **2022**, *14*, 51954–51964.

[26] An, Y. L.; Tian, Y.; Zhang, Y. C.; Wei, C. L.; Tan, L. W.; Zhang, C. H.; Cui, N. X.; Xiong, S. L.; Feng, J. K.; Qian, Y. T. Two-dimensional silicon/carbon from commercial alloy and CO_2 for lithium storage and flexible $Ti_3C_2T_x$ MXene-based lithium-metal batteries. *ACS Nano* **2020**, *14*, 17574–17588.

[27] Ren, Y.; Xiang, L. Z.; Yin, X. C.; Xiao, R.; Zuo, P. J.; Gao, Y. Z.; Yin, G. P.; Du, C. Y. Ultrathin Si nanosheets dispersed in graphene matrix enable stable interface and high rate capability of anode for lithium-ion batteries. *Adv. Funct. Mater.* **2022**, *32*, 2110046.

[28] Zhang, P.; Wang, X. D.; Zhang, Y. F.; Wei, Y.; Shen, N.; Chen, S.; Xu, B. Burgeoning silicon/MXene nanocomposites for lithium ion batteries: A review. *Adv. Funct. Mater.* **2024**, *34*, 2402307.

[29] Li, X.; Chen, Z. Y.; Li, A.; Yu, Y. C.; Chen, X. H.; Song, H. H. Three-dimensional hierarchical porous structures constructed by two-stage MXene-wrapped Si nanoparticles for Li-ion batteries. *ACS Appl. Mater. Interfaces* **2020**, *12*, 48718–48728.

[30] Xia, M. T.; Chen, B. J.; Gu, F.; Zu, L. H.; Xu, M. Z.; Feng, Y. T.; Wang, Z. J.; Zhang, H. J.; Zhang, C.; Yang, J. H. $Ti_3C_2T_x$ MXene nanosheets as a robust and conductive tight on Si anodes significantly enhance electrochemical lithium storage performance. *ACS Nano* **2020**, *14*, 5111–5120.

[31] Fu, N.; Liu, Z. J.; Shen, B. X.; Shao, W.; Wang, T. T.; Zhao, H. H.; Wang, J.; Chen, Q.; Luo, J. H.; Liu, Y. et al. Carbon and MXene dual confinement and dense structural engineering toward construct high performance micron-SiO_x anode for Li-ion batteries. *Adv. Funct. Mater.* **2024**, *34*, 2410839.

[32] Liu, N. N.; Yu, L. L.; Liu, B. J.; Yu, F.; Li, L. Q.; Xiao, Y.; Yang, J. H.; Ma, J. Ti_3C_2-MXene partially derived hierarchical 1D/2D TiO_2/Ti_3C_2 heterostructure electrode for high-performance capacitive deionization. *Adv. Sci.* **2023**, *10*, 2204041.

[33] Wang, F. K.; Wang, Z. Y.; Wang, S. D.; Meng, X. X.; Jin, Y.; Yang, N. T.; Sunarso, J.; Liu, S. M. Mechanically intensified and stabilized MXene membranes via the combination of graphene oxide for highly efficient osmotic power production. *J. Membr. Sci.* **2022**, *647*, 120280.

[34] Zheng, Y.; Shen, Y. Y.; Guo, J. P.; Li, J. D.; Wang, J.; Ning, D.; Liu, Y.; Huang, Y. K.; Tang, Y. X.; Deng, Y. H.; et al. Recent advances in solid-state lithium batteries based on anode engineering. *Nano Res. Energy* **2024**, *3*, e9120118

[35] Grimm, S.; Schweiger, M.; Eigler, S.; Zaumseil, J. High-quality reduced graphene oxide by CVD-assisted annealing. *J. Phys. Chem. C* **2016**, *120*, 3036–3041.

[36] Jakhar, R.; Yap, J. E.; Joshi, R. Microwave reduction of graphene oxide. *Carbon* **2020**, *170*, 277–293.

[37] Shi, H. Y.; Zhang, L.; Huang, X. H.; Kong, Q. Q.; Abdukayum, A.; Zhou, Y. T.; Cheng, G. Y.; Gao, S. S.; Hu, G. Z. Efficient catalysis for zinc–air batteries by multiwalled carbon nanotubes-crosslinked carbon dodecahedra embedded with Co–Fe nanoparticles. *Small* **2025**, *21*, 2409129.

[38] Ren, H. L.; Su, Y.; Zhao, S.; Li, C. W.; Wang, X. M.; Li, B. H. Construction of SiO_x–SnO_2 heterojunction and surface coating to achieve high-performance anode materials for lithium-ion batteries. *Electrochim. Acta* **2025**, *514*, 145688.

[39] Wu, P. F.; Guo, X. X.; Su, Z. M.; Liu, C.; Chen, S. H.; Zheng, Z. C.; Liu, A. H. Preparation of silicon oxycarbide (SiOC) anodes for high performance Li-ion batteries using competitive relationship between crosslinking and polymerization. *Chem. Eng. J.* **2022**, *446*, 137354.

[40] Lyon, J. T.; Andrews, L. Titanium, zirconium, and hafnium metal atom reactions with CF_4, CCl_4, and CF_2Cl_2: A matrix isolation spectroscopic and DFT investigation of triplet XC÷MX_3 complexes. *Organometallics* **2007**, *26*, 2519–2527.

[41] Fu, F. B.; Huang, Z.; Qiu, S. Y. SiO_x encapsulated into nitrogen-enriched lignin porous carbon for fast lithium storage. *Ind. Eng. Chem. Res.* **2025**, *64*, 2133–2144.

[42] Mani, G.; Feldman, M. D.; Oh, S.; Agrawal, C. M. Surface modification of cobalt-chromium-tungsten-nickel alloy using octadecyltrichlorosilanes. *Appl. Surf. Sci.* **2009**, *255*, 5961–5970.

[43] Tang, R.; Hu, Y.; Yan, J. Y.; Xu, S. Q.; Wang, Y. L.; Yan, J. S.; Liao, D. K.; Zhang, H. B.; Tong, Z. F. Multifunctional carboxylated cellulose nanofibers/exfoliated bentonite/Ti_3C_2 aerogel for efficient oil adsorption and recovery: The dual effect of exfoliated bentonite and MXene. *Chem. Eng. J.* **2023**, *473*, 145412.

[44] Zhang, D. M.; Zhang, G. L.; Liu, R. B.; Yang, R. N.; Li, X.; Zhang, X. Q.; Yu, H.; Zhang, P. X.; Li, B. W.; Hou, H. et al. Mutually activated 2D $Ti_{0.87}O_2$/MXene monolayers through electronic compensation effect as highly efficient cathode catalysts of Li–O_2 batteries. *Adv. Funct. Mater.* **2025**, *35*, 2414679.

[45] Sun, L.; Wang, L. J.; Liu, Y.; Wang, H. Y.; Jin, Z. Synergistic engineering of micron-sized porous silicon anodes via Ge doping and liquid metal alloy modification for high-energy-density lithium-ion batteries. *J. Mater. Chem. A* **2025**, *13*, 14346–14352.

[46] Xie, J.; Sun, L.; Liu, Y. X.; Xi, X. G.; Chen, R. Y.; Jin, Z. SiO_x/C-Ag

nanosheets derived from Zintl phase $CaSi_2$ via a facile redox reaction for high performance lithium storage. *Nano Res.* **2022**, *15*, 395–400.

[47] Zhang, Y. C.; Wu, Y.; An, Y. L.; Wei, C. L.; Tan, L. W.; Xi, B. J.; Xiong, S. L.; Feng, J. K. Ultrastable and high-rate 2D siloxene anode enabled by covalent organic framework engineering for advanced lithium-ion batteries. *Small Methods* **2022**, *6*, 2200306.

[48] Song, H. C.; Wang, H. X.; Lin, Z. X.; Jiang, X. F.; Yu, L. W.; Xu, J.; Yu, Z. W.; Zhang, X. W.; Liu, Y. J.; He, P. et al. Highly connected silicon-copper alloy mixture nanotubes as high-rate and durable anode materials for lithium-ion batteries. *Adv. Funct. Mater.* **2016**, *26*, 524–531.

[49] Rundla, A.; Priyanka; Kumar, B.; Tripathi, P.; Kumar, P.; Singh, K. $Ti_3C_2T_x$ MXene@rGO composite electrodes for high-performance supercapacitor applications. *J. Power Sources* **2025**, *632*, 236408.

[50] Zhao, L.; Li, Y.; Yu, M. M.; Peng, Y. Y.; Ran, F. Electrolyte-wettability issues and challenges of electrode materials in electrochemical energy storage, energy conversion, and beyond. *Adv. Sci.* **2023**, *10*, 2300283.

[51] Yang, F.; Deng, P. C.; He, H.; Hong, R. L.; Xiang, K.; Cao, Y.; Yu, B. B.; Xie, Z. M.; Lu, J. M.; Liu, Z. K. et al. Rapid joule heating-induced welding of silicon and graphene for enhanced lithium-ion battery anodes. *Chem. Eng. J.* **2024**, *494*, 152828.

This is an open access article under the terms of the Creative Commons Attribution 4.0 International License (CC BY 4.0, https://creativecommons.org/licenses/by/4.0/).

© The Author(s) 2026. Published by Tsinghua University Press.